Investigation of spatially localized defects in synthetic WS$_2$ monolayers

Bárbara L. T. Rosa [1,2] Kazunori Fujisawa,[3,4] Joyce C. C. Santos,[1] Tianyi Zhang,[4,5] Matheus J. S. Matos [6]
Frederico B. Sousa,[1] Tiago C. Barbosa [7] Lucas Lafeta [1] Sérgio L. L. M. Ramos,[7] Bruno R. Carvalho [8] Helio Chacham,[1]
Bernardo R. A. Neves [1] Mauricio Terrones,[3,4,9,*] and Leandro M. Malard [1,†]

[1]*Departamento de Física, Universidade Federal de Minas Gerais, Belo Horizonte, Minas Gerais 30123-970, Brazil*
[2]*Institut für Festkörperphysik, Technische Universität Berlin, Hardenbergstrasse 36, 10623 Berlin, Germany*
[3]*Department of Physics, The Pennsylvania State University, University Park, Pennsylvania 16802, USA*
[4]*Center for 2-Dimensional and Layered Materials, The Pennsylvania State University, University Park, Pennsylvania 16802, USA*
[5]*Department of Materials Science & Engineering, The Pennsylvania State University, University Park, Pennsylvania 16802, USA*
[6]*Departamento de Física, Universidade Federal de Ouro Preto, Ouro Preto, Minas Gerais 35400-000, Brazil*
[7]*CTNano, Universidade Federal de Minas Gerais, Belo Horizonte, Minas Gerais 31310-260, Brazil*
[8]*Departamento de Física, Universidade Federal do Rio Grande do Norte, Natal, Rio Grande do Norte 59078-970, Brazil*
[9]*Department of Chemistry and Materials Science & Engineering, The Pennsylvania State University,
University Park, Pennsylvania 16802, USA*

While the spatially nonhomogeneous light emission from synthetic WS$_2$ monolayers is frequently reported in the literature, the nature of this phenomenon still requires thoughtful investigation. Here, we combine several characterization techniques (optical imaging, scanning probe and electron microscopy) along with density functional theory to investigate the presence of substitutional doping localized at narrow regions along the S zigzag edge of WS$_2$ monolayers. We verified that photoluminescence quenching along narrow regions is not related to grain boundaries but to substitutional impurities of lighter metals at the W sites, which modify the radiative and nonradiative decay channels. We also found potential candidates for occupying the W site through ADF-STEM analysis and discussed their impact on photoluminescence quenching by performing density functional theory calculations. Our findings shed light on how atomic defects introduced during WS$_2$ monolayer's synthesis impact the crystalline quality and, therefore, the development of high-performance optoelectronic devices based on semiconducting 2D materials.

I. INTRODUCTION

Two-dimensional (2D) semiconductors belonging to the transition metal dichalcogenides (TMDs) family have demonstrated remarkable physical properties. Amid several of them, we highlight the indirect-to-direct band gap transition upon the thickness reduction from bulk to monolayers [1], circular-polarized light with valley selectivity [2], single-photon generation from single-defect states [3–6], and strong many-body interactions [7,8]. Furthermore, the synthesis of TMD single-crystal monolayers by chemical vapor deposition (CVD) with high quality and large area has been achieved, providing a step toward industrial-scale applications of these materials [9–13]. However, an inhomogeneity in photoluminescence (PL) response, as observed in mostly all synthetic TMD monolayers, has introduced a discussion about the crystalline quality of the synthesized flakes if compared to the exfoliated ones [14–18], where different factors, such as substrate interactions, strain fields, single defects, and grain boundaries [11,12,19–26], emerge as a synthetic growth after effects.

Several works have correlated the PL enhancement from edges of CVD-grown TMD monolayers to different mechanisms: The presence of localized states due to sulfur (S) vacancies [11,25], formation of biexcitons [21], or charge transfer by oxygen passivation of vacancies [19,27]. Some reports have further shown a more complex photoluminescence-enhanced emission pattern, ascribed to different charge concentrations along grain boundaries (GBs) in polycrystalline monolayers, which affects the PL quantum yield [14,20,28–32]. Moreover, an anomalous PL quenching, commonly seen as a narrow region from the center to the vertex of triangular-shaped tungsten disulfide monolayers (WS$_2$), has also commonly been associated with the presence of GBs [20,28–30], although there is no experimental confirmation of such statement in the literature that confirms the nature of well-defined narrow dark lines in synthetic WS$_2$ monolayers. On the other hand, An *et al.* [33] investigated the time evolution of CVD-WS$_2$ flakes morphology and attributed the existence of such narrow dark lines to the presence of W vacancies; however, a systematic study focusing on unraveling the nature of those PL quenching still requires further investigation.

Here, through several experimental techniques and theoretical calculations, we investigate the well-defined narrow dark regions, frequently observed in WS$_2$ monolayers along

*mut11@psu.edu
†lmalard@fisica.ufmg.br

the S zigzag edge, at which a PL quenching is observed. By performing second-harmonic generation (SHG) microscopy, combining bright- (BF) and dark-field (DF) imaging [34], we identified crystal grains and grain boundaries existing in our monolayers, which are not overlapped with regions showing PL quenching. This result suggests that the nature of dark regions is not due to grain boundaries but to other types of defects. Scanning probe microscopy (SPM) and scanning transmission electron microscopy (STEM) identified a high density of substitutional impurities at the tungsten (W) sites. Besides, STEM also provides different possible candidates for the W-atom replacements through annular dark-field imaging (ADF-STEM). Lastly, with the aid of spin-polarized density functional theory (DFT) calculations to investigate up to ten atoms and vacancies, we obtain information on defect formation energies with the electronic structure of defect states. The theoretical results highlight, among all candidates, the favorite atoms to occupy the W site of WS_2 and how they affect the PL emission. Our findings unfold the presence of substitutional impurities in synthetic TMDs, disentangling those defects from GBs and foremost revealing the nature of luminescence-quenching carrier trapping in CVD-grown monolayers of WS_2.

II. EXPERIMENTAL AND COMPUTATIONAL DETAILS

A. Sample synthesis

WS_2 flakes investigated in this work were grown on a SiO_2 (300 nm)/Si substrate by an atmospheric pressure CVD method [35]. The process consists of mixed WO_3 and NaBr powders (10 : 1 weight ratio) placed inside a porcelain boat, and a piece of one-side polished SiO_2/Si substrate positioned on top of the boat with the polished side facing down, where the CVD flake was grown. Later, sulfur powder (300 mg) was deposited in another porcelain boat located in the upstream. During the synthesis, substrate and mixed WO_3/NaBr powders were heated up to 800 °C by the tube furnace and held for 15 min, while the sulfur powder was heated up to 220 °C independently by a heating belt. After the reaction, the furnace was allowed to cool down naturally. An argon flow of 100 sccm was used through the process.

B. Optical spectroscopies and microscopies

Fluorescence imaging was performed using an Olympus BX51 fluorescence microscope at ambient conditions. Light from a Hg lamp passes through a bandpass filter 530–550 nm and heads to the objective and onto the sample by a dichroic mirror (with edge at 570 nm). Fluorescence response emitted by the sample travels back through the objective and the dichroic mirror before passing through a long-pass filter 590 nm, and is then directed into the camera system. Photoluminescence and Raman spectroscopies were performed using a WiTec Alpha 300 at ambient conditions. The sample was excited with a Nd:YAG laser with wavelength of 532 nm with an excitation power of 0.5 mW onto the sample. The laser was focused by a $100\times$ objective with 0.9 NA. The signal was recorded through a 532 nm long-pass filter, using the same objective and a grating of 600 grooves mm^{-1}. For this

configuration, the spot size approaches the diffraction limit of 250–300 nm.

Second-harmonic imaging was performed by scanning the laser with a set of galvanometric mirrors (Lavision Biotec) in a modified Nikon microscope. The laser system used was an optical parametric oscillator (APE PicoEmerald) with 80 MHz repetition rate, 7 ps pulse width tuned at 810 nm. The near-infrared laser was directed to the microscope and then focused onto the sample by a $40\times$ objective (0.95 NA). The backscattered second-harmonic signal was reflected by a dichroic mirror that reflects below 690 nm followed by a bandpass filter that selects only wavelengths corresponding to the second harmonic that is then detected by an enhanced GaAsP photomultiplier tube (PMT). For dark-field second-harmonic imaging, a dark-field filter (patch stop) was inserted before the PMT detector as shown in Ref. [34].

C. Scanning probe and electron transmission microscopies

SPM measurements were carried out with a Bruker MultiMode8 SPM. For AFM characterization, intermittent contact and PeakForce modes were conducted using a HQ:NSC15/AL-BS (MikroMash) cantilever. Lateral force microscopy (LFM) measurements were performed by using a RC800PSA (Olympus) cantilever. We calculated the LFM signal as the difference in lateral torsion between scans in forward (trace) and backward (retrace) directions, which enhances the friction difference and minimizes topographic artifacts. We also performed electrostatic force microscopy (EFM) and scanning Kelvin probe microscopy (SKPM) experiments by using AC240-TM (Pt-coated tip) cantilever from Olympus. The EFM and SKPM experiments were carried out at a fixed lift height (50 nm) above the sample surface. Lastly, SKPM imaging was performed with an AC bias $V_{AC} = 2$ V applied to the probe at the resonant frequency of the cantilever. We performed all experiments at ambient conditions.

STEM measurement was carried out by using an FEI Titan3 G2 S/TEM 60–300 with a spherical aberration corrector on both the probe- and the image-forming lens at an accelerating voltage of 80 kV. ADF-STEM image simulation was performed by QSTEM software developed by Koch [36]. All parameters for the ADF-STEM image simulation were appropriately set according to experimental imaging conditions, including the acceleration voltage, spherical aberration (C_3 and C_5), convergence angle, and inner/outer angle for the ADF detector. For most images in this work, a Gaussian blur filter ($r = 0.03$ nm) was applied by the ImageJ [37] program to reduce noise and therefore enhance the visibility of the structural details. ADF-STEM intensity analysis was performed by the ImageJ [37] program on processed images by the Gaussian blur and bandpass filter [see Fig. S8 in the Supplemental Material [48] (SM)]. Here, a bandpass filter was employed to reduce the contrast from carbon contamination on the surface of WS_2 structure. To obtain total ADF intensity from an atom, the atom was overlaid with a circular region-of-interest (ROI) with a diameter of 0.2 nm, and the ADF-STEM signal within the ROI was summed. More than 16 000 metal sites (approximately 40×40 nm^2) are used in ADF-STEM intensity analysis to accurately count the concentration of

impurity with ppm order accuracy. The same process was applied to simulated ADF-STEM images.

D. Density functional theory calculations

We performed *ab initio* calculations based on the density functional theory [38,39] as implemented in the SIESTA code [40,41]. The generalized gradient approximation (GGA/PBE) was chosen for the exchange-correlation functional [42]. We make use of a relativistic norm-conserving Troullier-Martins pseudopotentials [43,44] in the Kleinman-Bylander factorized form [45] and a double-ζ basis set composed of finite-range numerical atomic pseudofunctions enhanced with polarization orbitals. Spin polarization was included in all calculations. A real-space grid was used with a mesh cutoff of 350 Ryd and the Brillouin zone was sampled using a $4 \times 4 \times 1$ k-grid Monkhorst-Pack [46]. All geometries were optimized so that the maximum force on any atom is less than 10 meV Å^{-1}. Optical absorption spectrum was calculated using dipole transition matrix elements between Kohn-Sham states with a grid of $10 \times 10 \times 1$ k points for energies up to 4 eV. A Gaussian broadening with width of 0.05 eV was used in the absorption spectrum. We employed a 10×10 supercell model containing 300 atoms. Formation energy was calculated using the following expression

$$E_{\text{form}} = E_{\text{cell}} - E_{\text{pristine}} + \mu_W - \mu_M, \quad (1)$$

where E_{cell} and E_{pristine} are the total energies of the large unit cell that includes the defect and the pristine case, μ_W is the chemical potential calculated from the total energy of a perfect bcc tungsten crystal, and μ_M is the chemical potential of the substitutional transition metal. In this case, we choose the fcc structure for Sc, Y, and Mn and bcc for Cr, Mo, Nb, V. For Ga we use the bct structure. All graphics of atomistic models and charge densities plots were performed with XCrySDen [47].

III. RESULTS AND DISCUSSION

A. Photoluminescence characterization

Figures 1(a)–1(f) show optical and fluorescence images (FI) of a set of different CVD-grown WS_2 monolayers. Bright-field images shown in Figs. 1(a)–1(c) reveal the homogeneity of our monolayers, except for the presence of nucleation sites located at the center of these polycrystalline flakes [Figs. 1(a) and 1(b)]. The corresponding FI images [Figs. 1(d)–1(f)] exhibit distinct emission intensities throughout the flakes (see Fig. S1 in the Supplemental Material [48] for more bright-field and FI images of other flakes). It is noteworthy that all flakes exhibit a PL quenching along darker and narrow lines, going from the center to the triangle vertices in both polycrystalline [Figs. 1(d) and 1(e)] and monocrystalline samples [Fig. 1(f)]. The decrease in PL intensity in these narrow regions is about 30%, as shown by the intensity profile in the inset of Fig. 1(f) (see Supplemental Material [48], Fig. S2, for more information). We also observe a stronger light emission at the edges and the bright regions at the interface between domains of polycrystalline monolayers [Figs. 1(d) and 1(e)]. To clarify the following discussion, we label those distinct sharp lines as *dark regions* and *bright regions*, the latter being commonly reported in the literature as S vacancies interacting
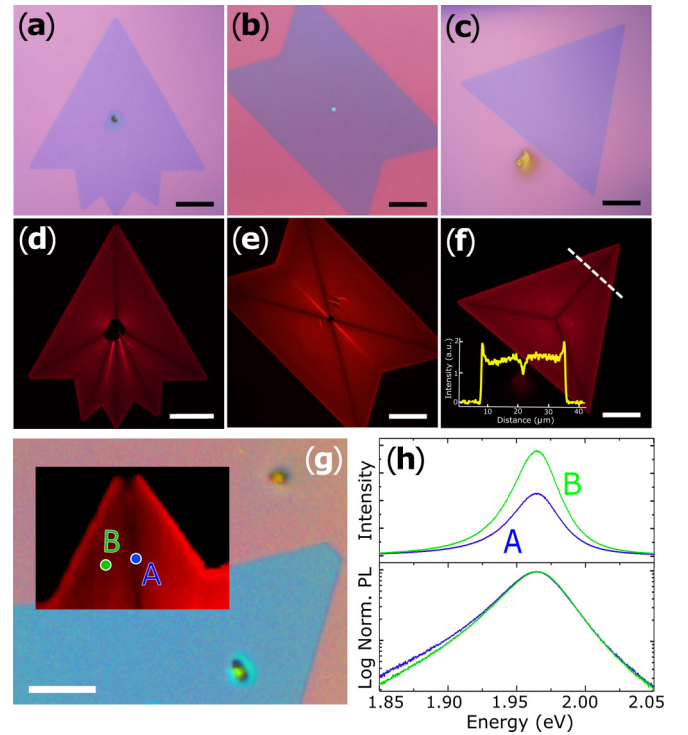

FIG. 1. (a)–(c) Optical images of different synthesized WS_2 monolayers. (d)–(f) Respective FI images. The intensity profile collected from the white dashed line in (f) is seen in the yellow inset graph. Scale bar: 20 μm. (g) Optical image of a star-shaped WS_2 monolayer with the overlaid hyperspectral PL intensity image. Scale bar: 10 μm. (h) Top: PL spectrum taken at regions A (blue) and B (green) shown in (g). Bottom: Normalized PL spectrum at positions A (blue) and B (green) in (a) shown in logarithmic scale.

with environment molecules (e.g., oxygen) [20,23]. Nonetheless, in this work, we aim attention at the local PL quenching and, therefore, will omit further discussion of bright regions unless required to explain the presence of the dark regions.

The hyperspectral PL imaging performed in a polycrystalline WS_2 monolayer is shown in Fig. 1(g). The spectra collected from the dark region and the pristine region at points A and B, respectively, were acquired at room temperature (RT) using 532-nm laser excitation. The typical peak shape for pristine CVD-WS_2 monolayers, consisting mainly of neutral-exciton peak X^0 at $E_{X_0} \sim 1.97$ eV, agrees with optical properties of undoped CVD-WS_2 monolayer [22,25,49]. The absence of trionic and biexcitonic emissions was also confirmed via excitation power dependence measurements (see Supplemental Material [48], Fig. S3). As reported in the literature, TMD monolayers may change the complex excitonic response, such as the appearance of trions and biexcitons, depending on the power excitation intensity at which the flakes are exposed [22,50]. Carrying out power dependence series measurements in our samples, we observe that a predominant single peak (Fig. S3) remains approximately at constant energy emission (~ 1.97 eV), showing only a slightly broadening of spectra under power excitation at an energy below 1.93 eV, which may be attributed to local heating effects.

To investigate the presence of local strain, we performed Raman spectroscopy on the dark region and the pristine region

(Supplemental Material [48], Fig. S4). As a result, the Raman spectra show no detectable peak shifts between the dark and pristine regions (see Supplemental Material [48], Fig. S4), which has been assigned as a trustworthy indicator of strain in 2D materials [51–53]. Along with an unchangeable PL peak position shown in Fig. 1(g), we suggest that dark regions can be considered an unstrained region in comparison with pristine regions nearby [53–55].

It has also been reported that S vacancies observed in synthetic monolayers may alter the PL intensity response. As reported by Carozo *et al.* [25] in a similar sample, a defect-bound exciton emission showing low emission energy (1.65 eV) is expected at liquid nitrogen temperature when S vacancies are isolated. Thus, to rule out the existence of dark regions as a consequence of S vacancies, we performed room and nitrogen temperature (77 K) fluorescence imaging by using different bandpass filters (see Fig. S5). The fluorescence images at room and low temperature exhibit a stronger PL emission on the WS_2 monolayer edges Figs. S5(b) and S5(c), respectively when the selected energy emission is 1.97 eV. However, when the bandpass filter is centered at 1.65 eV, bound-exciton emission is only detected along the edges of the WS_2 monolayer at 77 K, whereas no PL response is observed along the line from the center to the vertex of the flakes (dark regions) Fig. S5(d). It suggests, therefore, that the responsible mechanism for decreasing the excitonic emission in the dark regions is likely not to be related neither to the presence of isolated S vacancies nor to local strain [32,53,56,57], but rather to other defects that introduce different recombination channels in TMD monolayers [23,58–60].

B. Second-harmonic generation

To retrieve information about the nature of dark regions, we carried out polarization-resolved SH measurements and dark-field SH imaging, as shown in Fig. 2. Regions I (black arrows) and II (red arrows), highlighted in Figs. 2(a)–2(c), correlate respectively to the dark and bright regions as seen by the inset of the FI images, corresponding to Figs. 1(d)–1(f). The second-harmonic generation technique has been used as a powerful tool to identify the structural properties of exfoliated and CVD-synthesized 2D materials [34,61–66], because of the inversion symmetry absence in TMD monolayers that leads to a finite second-order nonlinear susceptibility $\chi^{(2)}$. Moreover, in addition to being a rapid method for identifying monolayers and odd-few layers TMDs, and crystallographic orientation [61–63], SH imaging allows us to identify grain boundaries in polycrystalline CVD flakes [34,64], named in our work as bright regions.

The generated SH electric field amplitude depends on the crystallographic orientation of the sample concerning the incident laser polarization [61]. Thus, by placing a polarizer in front of the detector, different grain orientations will show different SH intensities [61–64]. From Figs. 2(a)–2(d), one notices that WS_2 grains reveal distinct SH intensities, indicating the formation of boundaries between individual grains (regions II). Although the SH intensity remains the same in Fig. 2(b), the interference between the generated SH electric fields with the opposite phases due to 180° of rotation between the WS_2 grains leads to a suppression of the SH response
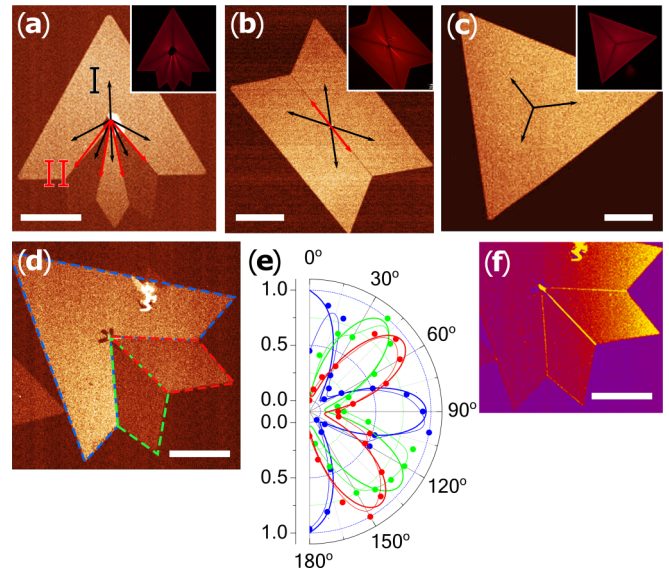

FIG. 2. (a)–(d) Polarized-resolved SH imaging on different WS_2 monolayers. Labels I and II, black and red arrows, respectively, indicate regions exhibiting the dark and bright regions shown in the inset FI images. (e) SH intensity as function of input laser polarization angle for the three different domains shown in (d). (f) Dark-field SH imaging of the WS_2 flake shown in (d). Scale bar: 30 μm.

at the grain boundary (region II) [64]. Figure 2(e) shows the acquired SH polarized-resolved intensity for three WS_2 grain domains highlighted in Fig. 2(d). The single grains 1 (red dashed line), 2 (green dashed line), and 3 (blue dashed line) exhibit distinct orientations when looking at the polycrystal, where angles of 12°, 21°, and 9° were recorded between the crystals 1–2, 2–3, and 3–1, respectively (details regarding the fitting procedure can be found in the SM [48], Sec. 6 and Fig. S6). The absence of difference in SH emission intensities through regions I, as indicated in Figs. 2(a)–2(c), on the other hand, indicates negligible GB presence.

Furthermore, we conducted dark-field SH imaging in this flake to visualize better the GBs localized between these three WS_2 single crystals that compose the polycrystalline monolayer. This technique reveals GBs and edges within TMDs by suppressing SH signal from the monolayer region and thus enhancing the SH signal from the GBs between the domains, as discussed by Carvalho *et al.* [34]. In Fig. 2(f), one can observe the emission from GBs and therefore the presence of bright regions (regions II) that coincide with GBs, as previously reported [20,23]. In contrast, the absence of dark-field SH response along the dark regions (regions I), reinforced by bright-field images [Figs. 2(a) and 2(b) and 2(c)], strongly suggests that at this region no grain boundaries were formed during CVD monolayer growth.

C. Scanning probe microscopy

We next explored the surfaces of the dark regions by employing a series of SPM imaging techniques—atomic force microscopy (AFM), scanning Kelvin probe microscopy (SKPM), electrostatic force microscopy (EFM), and lateral force microscopy (LFM). Figures 3(a) and 3(b) show the FI
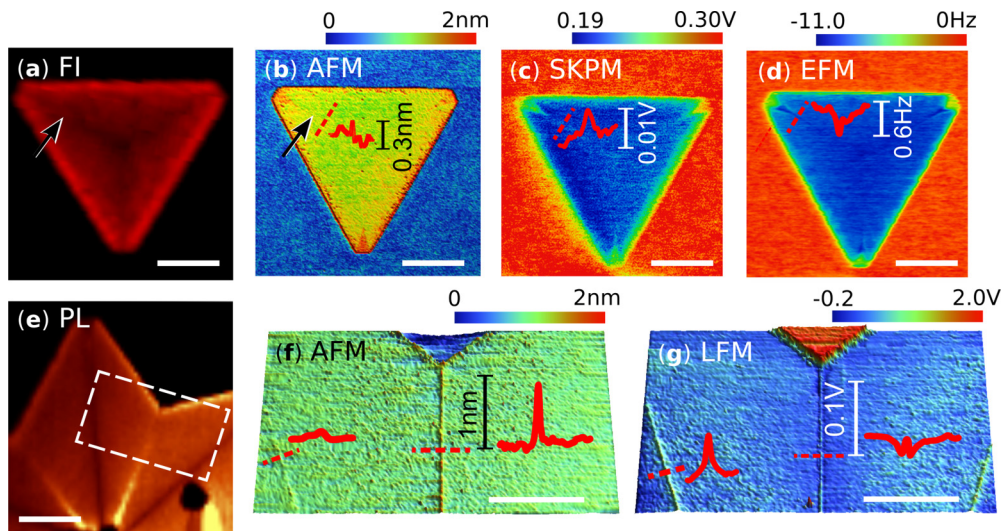
FIG. 3. (a) FI image of a triangular-shaped WS_2 monolayer grown on SiO_2/Si. Scale bar: $15\,\mu m$. (b) AFM image of the flake displayed in (a). The black arrow indicates the topography profile from the dark region. (c) SKPM mapping of the surface potential of this same flake. (d) EFM image of the same flake acquired at tip bias $V_{tip} = -3$ V. Scale bar (a)–(d): 5 μm. (e) PL image of a WS_2 polycrystal on SiO_2/Si. The highlighted rectangular region indicates the region where AFM and LFM were recorded. Scale bar: 12 μm. (f) AFM and (g) LFM image of the rectangular highlighted in (e). Scale bar in (f) and (g) corresponds to 10 μm. Dashed red lines in (f) and (g) indicate where line profiles (shown by full red lines) were measured.

and AFM images of a representative triangular WS_2 monolayer (in yellow-green shades) grown on SiO_2/Si (blue color at the AFM image). While dark regions do not show noticeable variations in the flake topography [Fig. 3(b)], they are revealed in the SKPM [Fig. 3(c)] and EFM [Fig. 3(d)] images. The dark regions are indicated by light blue lines in the SKPM image [Fig. 3(c)], which shows a higher surface potential than their neighboring region (highlighted by the profile in red). These same dark regions appear as negative contrast background (when compared to the flake's signal) in the EFM image [Fig. 3(d)], which indicates an intensified EFM signal response (negative frequency shift, as shown by the profile in red). In semiconducting materials, an increase in the surface potential measured via SKPM suggests a decrease in its work function value, which is commonly associated with doping of the material [67–69]. Additionally, a larger magnitude frequency shift in EFM images is indicative of a high dielectric constant (for the same sphere-plane capacitor approximation) [67,69]. Among several possibilities for enhancing the dielectric constant of a given material, doping and substitutional defects are the most expected [67–69]. Therefore, SKPM and EFM images jointly demonstrate that dark regions have different electrical properties than their surrounding flake (lower work function and higher dielectric constant), consistent with either doping or compositional variations at the dark regions.

In addition to electrical characterization, SPM allows simple structural analysis of WS_2 monolayers via LFM imaging [28,67]. Figures 3(f) and 3(g) exhibit the topography (AFM) and friction (LFM) images of a selected area of a star-shaped WS_2 monolayer, as shown in Fig. 3(e) (see dashed square), where both dark regions and bright regions are present. Only a small fraction of the substrate (in blue shades) is seen in Fig. 3(f), while most of the green regions

in the image correspond to the WS_2 monolayer. One can identify the bright region, where a grain boundary is located, at the image center by its different height, being several angstroms thicker than its surrounding, as indicated by the line profile shown in Fig. 3(f). The dark region, nevertheless, produce significantly smaller AFM topography variations (0.1–0.2 nm) when compared to the bright regions, whether in single or polycrystalline WS_2 monolayers [Figs. 3(b) and 3(f), respectively], despite the edges in the triangular-shape flake [Fig. 3(b)].

Figure 3(g) depicts the friction image of the same area, where a noticeable difference in friction coefficients between the WS_2 monolayer (in blue shades) and the SiO_2/Si (in red) are revealed. We can also observe two diagonal lines near both the left and right sides of the image edges corresponding to the dark regions, whereas the line at the center corresponds to the bright region [see Fig. 3(e)]. By performing a line scan [dashed red line in Fig. 3(f)] across the dark and bright regions and comparing their relative friction intensities, we consider that the tip-sample friction coefficient is noticeably larger at the dark region than in the bright region. Our SPM results agree with the SH results already discussed here, suggesting that dark and bright regions arise from different mechanisms, with the latter being ascribed as a grain boundary. In addition, combined SKPM, EFM, and LFM results may lead us to consider that dark regions' presence is rather a result of local chemical compositional variations [28,67].

D. Transmission electron microscopy

In order to investigate the possible chemical compositional variations in the dark regions, we performed annular dark-field imaging using scanning transmission electron microscopy (ADF-STEM). Figure 4(a) shows a FI image of a
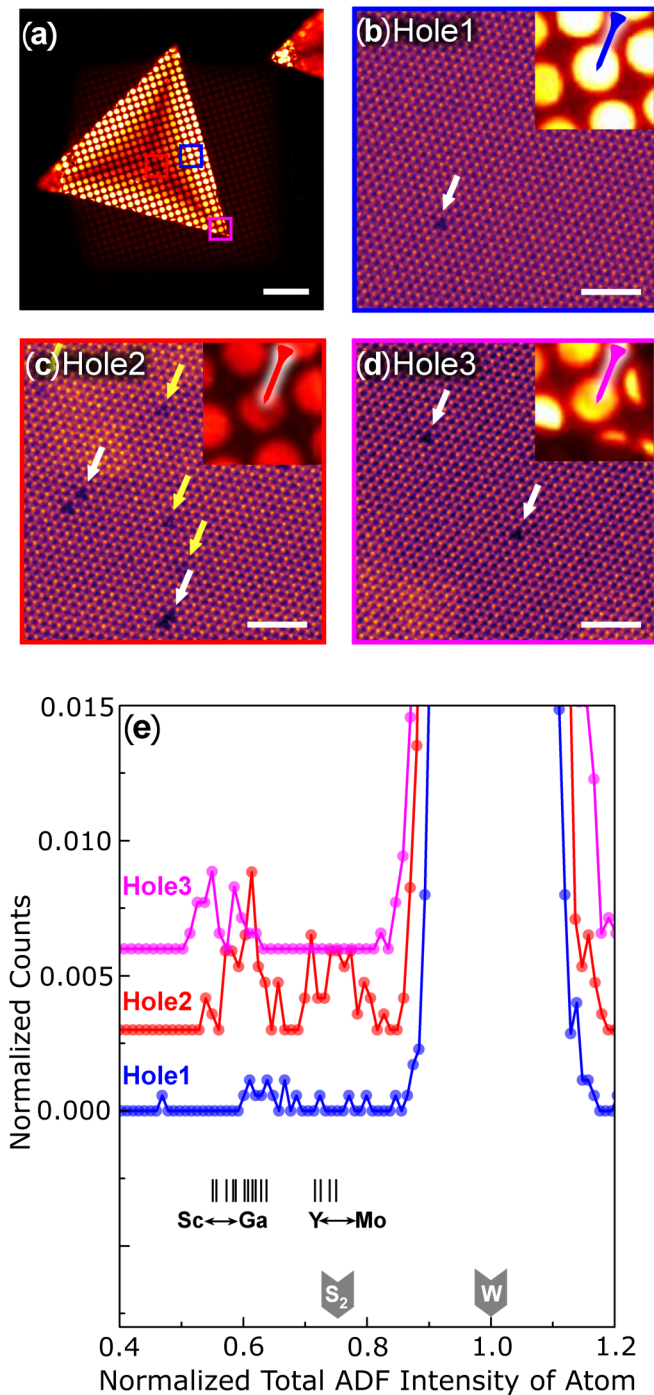
FIG. 4. (a) FI image of a triangular WS_2 monolayer transferred on top of a TEM grid. Scale bar: 20 μm. (b)–(d) Scanning transmission electron microscopy (STEM) images taken at the regions shown by holes 1, 2, and 3 shown in (a). Scale bar: 2 nm. Insets showing magnified FI image and the pins indicate the location investigated by STEM. (e) Histogram of total ADF intensity of atom. The total ADF intensity was collected from a circular area with a diameter of 0.2 nm around an atom. The obtained total ADF intensities were normalized using W and S_2 signals as 1.00 and 0.75, respectively. Profiles from holes 2 and 3 are shifted vertically for visibility. The vertical lines in bold correspond to the normalized total ADF intensity of substitutional lighter transition atoms incorporated into the W-site of the WS_2 monolayer, obtained from STEM simulations.

triangular WS_2 monolayer transferred to a TEM grid. Figure 4(b) is the ADF-STEM with atomic resolution at holes 1 (blue square) shown in Fig. 4(a) that are located outside the dark regions, while Figs. 4(c) and 4(d) reveal the STEM image at hole 2 (red square) and hole 3 (pink square), respectively, along the dark regions. In this particular imaging mode, the contrast changes depending on $Z^{1.7-1.8}$; thus the "darker" atoms in the ADF-STEM image indicate that tungsten (W) atoms are substituted by lighter atoms. It is worth noting that no grain boundary was detected along the dark regions, but a higher density of such substitutional defects (see SM [48], Fig. S7). The large number of dark dots at dark regions in the ADF-STEM results [Figs. 4(c) and 4(d)] confirms the presence of substitutional defects, as verified by the LFM results [see Fig. 3(g)]. Moreover, our findings indicate that the ADF-STEM results at the dark regions exhibit two different types of dots with lower and higher ADF signals, which are highlighted by white and yellow arrows, respectively, in Figs. 4(b)–4(d).

To figure out which elements may be substituting tungsten, we analyzed the ADF-STEM image intensity shown in Fig. 4(e) (see Sec. II C). In brief, a total ADF intensity of an atom is obtained by summing ADF signals over a circular area with a diameter of 0.2 nm around the atom. The total ADF intensities are normalized using signals from W and S_2 as 1.00 and 0.75, respectively, for comparison between images. The atomic concentration of impurities at W sites was calculated as 840 ppm, 4876 ppm, and 1269 ppm at hole 1, 2, and 3, respectively. Two peaks corresponding to atoms with light-gray, and dark-gray colors also appeared in the ADF-STEM intensity histogram. For holes 1 and 3, only one peak appeared, whereas two peaks are found in the case of hole 2. The peak for the lower ADF signal dark dots appeared at around 0.6 of the total ADF intensity of atom, while the peak for higher ADF signal dark dots was located at around 0.8, which is close to the value from the S_2 site.

To better understand this behavior, we also performed STEM simulations. Since the STEM image showed many dark dots in dark regions, here we only considered substitutional impurities—scandium (Sc) to gallium (Ga) for first-row transition metals (1st TMs), and yttrium (Y) to molybdenum (Mo) for second-row transition metals (2nd TMs)—at the W site. The values of the normalized total ADF intensity of atoms for the 1st TMs and 2nd TMs are closely located to the peaks for lower and higher ADF signal dark dots [see vertical bars in Fig. 4(e)]. Therefore, we assume that both 1st TMs and 2nd TMs are incorporated along the dark regions. For $Mo_{1-x}W_xS_2$ alloy systems, Mogi *et al.* [70] reported that Mo atoms are segregated along the line-shaped dark region. But in our case, all the impurities are derived from the growth system and/or reagent used to grow WS_2, similarly to Ref. [71]. We confirm our findings as impurity rather than alloy composition due to the Raman spectroscopy where only the peaks assigned to WS_2 are observed (see Supplemental Material [48], Fig. S4), differing from the results reported by Mogi *et al.* [70] in which MoS_2 Raman modes are also observed at the alloy regions. Nevertheless, such ppm order of substitutional impurities at the W site observed in our samples modifies the excitonic recombination mechanisms, therefore quenching the PL along the dark regions [23,58–60].
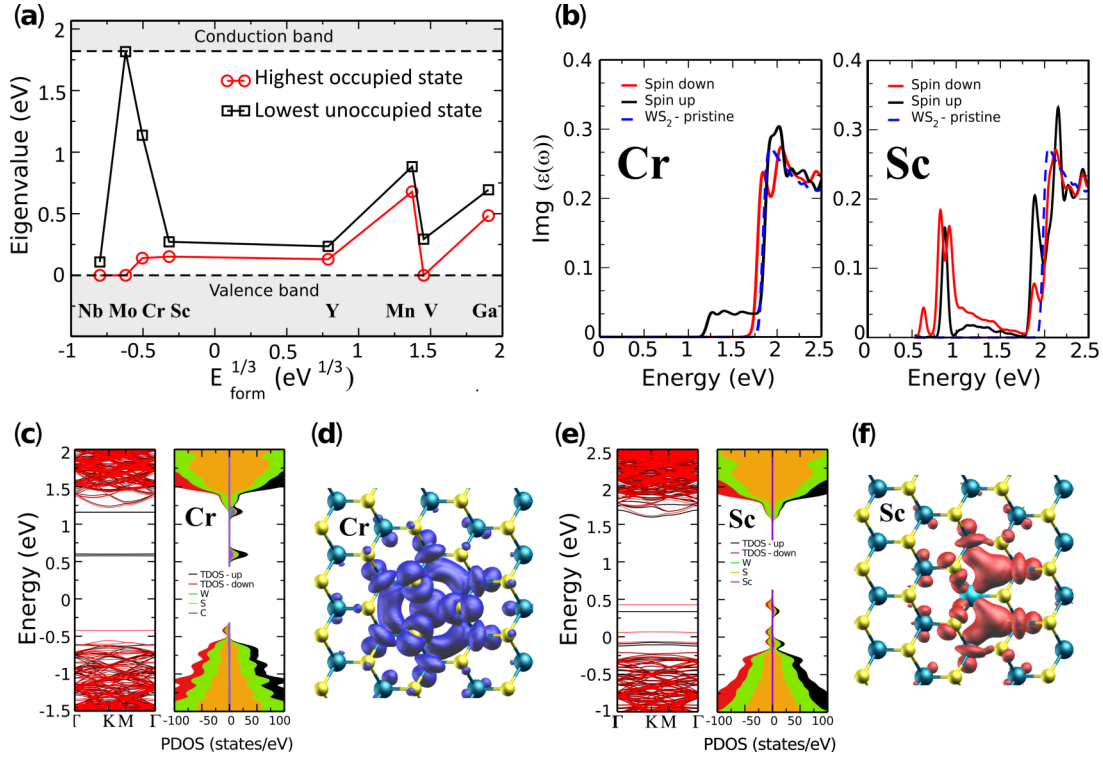
FIG. 5. (a) Eigenvalues of the highest occupied (red circles) and the lowest unoccupied (black rectangles) defect states versus the cubic root of the calculated formation energies of selected substitutional impurities in WS_2. (b) Imaginary part of the dielectric function as a function of energy for the Sc and Cr impurities. Spin-down (red line) and spin-up (black line) contributions are shown separately, and the response of pristine WS_2 (blue line) is also shown for comparison. (c), (e) Calculated electronic structure of the substitutional Cr and Sc impurities, respectively. Left: Calculated band structure, relative to the Fermi level, for the spin-down (red line) and spin-up (black line) states of the large unit cell containing the impurity. Right: Total density of states (TDOS), and projected density of states (PDOS) at selected atoms. (d), (f) Probability density of the lowest unoccupied states induced by the Cr (c) and Sc (e) impurities.

E. Density functional theory calculations

1. Formation energy and optical properties

Although our results may not determine a specific dopant responsible for the dark regions' formation, it is worth discussing the origins of the PL quenching for the different defects presented here. Consequently, in order to allow a deeper insight into our experimental findings, we also performed spin-polarized density functional theory (DFT) calculations for several substitutional impurities at the W site of single-layer WS_2 that were considered possible candidates in the above STEM analysis, namely, Nb, Mo, Cr, Sc, Y, Mn, V, and Ga. The calculation results presented here (see Sec. II D and SM [48], Secs. S8 and S9) provide information on defect formation energies and the electronic structure of defect states within the WS_2 band gap, supporting the identification of possible mechanisms responsible for the luminescence reduction at the dark regions.

Figure 5(a) shows the calculated eigenvalues of the lowest unoccupied (LUMO) and the highest occupied (HOMO) defect-induced electronic states within the WS_2 band gap as functions of the cubic root of the calculated formation energies ($E_{form}^{1/3}$) of several substitutional impurities at the W site. This figure contains two important types of information that arise from the calculations. First, E_{form} is an indicator of the stability of the defect: The smaller E_{form}, the smaller the energetic costs for its occurrence. Indeed, the defects with the smallest calculated E_{form} value in the figure (Nb, Mo, and Cr) are experimentally observed [71–73]. Second, the existence of HOMO and/or LUMO eigenvalues within the band gap are indicators of the possible action of the defect as an electron and/or hole trap, respectively, which could lead to luminescence reduction due to the reduction of free carriers. The figure shows that all the considered defects could, in principle, act as carrier traps, except for the Mo impurity, which does not induce defect states in the band gap. In the following paragraphs, we will discuss the four most stable substitutional impurities accordingly to Fig. 5(a), which are Nb, Mo, Cr, and Sc, emphasizing the Cr and Sc impurities afterward since they have been weakly explored in the literature.

The substitutional impurity Nb has the lowest calculated defect formation energy, and it induces an unoccupied state in the gap (see Figs. S13 and S14 for more details), which may lead it to stand as a candidate for a luminescence-quenching carrier trap. However, a previous experimental study [72] has shown that the substitutional doping of CVD-WS_2 monolayers with Nb at the W site promotes a strong redshift in the excitonic emission that was not observed in our PL measurements [Fig. 1(h)]. Nonetheless, since the dark lines exhibit a narrower lateral size in comparison with the laser spot, a PL contribution from the surrounding WS_2 pristine may hinder any energy shift induced by Nb impurity, and consequently, we cannot rule Nb out as a viable substitutional impurity in our samples.

The second most stable substitutional impurity in Fig. 5(a) is Mo. According to the results of our calculations shown in Fig. 5(a) and in Figs. S13 and S14 and Table S1 of the SM [48], the Mo impurity does not induce either defect states in the band gap or significant changes in the absorption spectrum compared to pristine WS_2. Our results are consistent with those of Ref. [71], where neither experiment nor theory indicates the existence of defect states in the gap induced by substitutional Mo at the W site. We therefore suggest that the available experimental and theoretical data exclude this impurity as a possible candidate for the luminescence quenching.

Following, the third most stable substitutional impurity in Fig. 5(a) is Cr. The Cr-induced HOMO and LUMO states also shown in this figure, as well as the full band structure of the defect and its impurity-projected density of states shown in Fig. 5(c), show that substitutional Cr at the W site induces deep unoccupied states in the band gap and an occupied state near the valence band maximum, which indicates that Cr might act as a deep electron trap. This result is consistent with Schuler *et al.* [71], where both DFT calculations and scanning tunneling spectroscopy measurements show the existence of unoccupied defect states in the band gap induced by substitutional Cr at the W site of WS_2. Therefore, our calculation places Cr as a solid candidate for a luminescence-quenching electron trap in the dark regions of our samples.

Substitutional Sc at the W site is the fourth most stable substitutional impurity in Fig. 5(a). The calculated band structure of the defect and its impurity-projected density of states, indicated in Fig. 5(e), show that Sc induces deep unoccupied states in the band gap and occupied states near the valence band maximum. This indicates that, similarly to Cr, Sc might act as a deep electron trap, placing Sc as a possible candidate for a luminescence-quenching electron trap. An interesting feature of the Sc defect, shown in Fig. 5(b), is that the probability density of the lowest unoccupied state only possesses the mirror symmetry across the horizontal line that passes through the Sc atom in the figure, while the point group symmetry at the cation sites in pristine single-layer WS_2 is C_{3v}, with additional mirror and $2\pi/3$ rotation symmetry operations. In contrast, the probability density of the Cr-induced lowest unoccupied state, shown in Fig. 5(f), does not depict such symmetry breaking. The origin of the symmetry breaking of the Sc state is a symmetry-breaking distortion of the lattice near the defect, shown in Figs. S16, S17, and S18, which is caused by the splitting of the nearly degenerate HOMO and LUMO states of the defect in an undeformed geometry (Fig. S13).

Figure 5(b) shows the DFT-calculated imaginary part of the dielectric function as a function of energy for the Sc and Cr substitutional impurities at the W site of WS_2. The calculations are made for spin-down (red line) and spin-up (black line) separately, and the same response is shown for pristine WS_2 (blue line) for comparison. The calculated DFT dielectric responses do not include many-body electron-electron or electron-hole corrections to DFT and therefore must be taken at most as semiquantitative estimates of absorption spectra and, to some extent, of luminescence spectra. Having taken that caution into consideration, Fig. 5(b) indicates that Sc and Cr might possess very different absorption and luminescence spectra. The Cr-induced response has a weak and broad fea-

ture in the visible region below the conduction band, without sharp and intense peaks. In contrast, the Sc-induced response has strong and sharp features in the infrared region. Such result suggests that luminescence arising from Sc defect might require detection in the infrared region below 1 eV, and that the luminescence arising from Cr might have low intensity. It is worth highlighting that although the other possible dopants suggested by ADF-STEM simulation (Y, Mn, V, and Ga) have higher E_{form}, they may incorporate into the lattice under appropriate growth conditions [74]. In this case, the dopants will alter the PL response similar to either the case of Cr or Sc, because those impurities create unoccupied midgap states (see Figs. S13 and S14).

Additionally, we noticed that some S vacancies might be coupled with transition metals incorporated into the WS_2 monolayer, as shown in Fig. S9. Spin-resolved DFT calculation was also performed considering, likewise, the coupling of TMs with one and two S vacancies, as displayed in Fig. S15 in a specific case of Cr as the dopant. There, we identified the formation of new unoccupied defect states in the band gap of WS_2, similarly to the results obtained without considering the coupling with S vacancies. Those defects can therefore be responsible for a PL quenching along the dark regions of our samples.

Our theoretical results provide information on defect formation energies and the electronic structure of defect states within the WS_2 band gap, supporting the identification of possible mechanisms responsible for the luminescence reduction in the dark regions. Nonetheless, we stress that though our STEM analysis sheds light on identifying possible candidates as substitutional defects responsible for an excitonic response suppression, as seen in all fluorescence images, we cannot address an assertive statement to differ both yellow and white substitutional atoms observed in the ADF-STEM image, Figs. 4(b)–4(d).

2. Mechanism behind the defect formation along the narrow regions

Concerning the spatial localization of substitutional defects, specifically the dark regions observed from the corners of the triangular flakes toward the center, we shed light upon the possible mechanisms behind it by performing DFT calculations. These theoretical results are described in Sec. S8 of the Supplemental Material [48]. The calculations performed for finite WS_2 triangular flakes demonstrate that both corners and edges of WS_2 flakes can depict non-crystal-like local structures. We also considered the possible removal of W atoms from flake corners, flake edges, and bulk regions in the calculations. Our results clearly show that the removal of W atoms from flake corners requires much less energy than the removal from flake edges. We also show that the removal of W atoms from the flake, either corners or edges, requires much less energy than the removal of W atoms from bulk regions. Therefore, from the energetic point of view, our calculations indicate that the formation of W vacancies is more likely to occur along the lines connecting the triangle corners to the triangle center, which coincides with the observed dark lines' locations. Lin *et al.* [23] argued that the distribution of various types of substitutional impurities in CVD-grown

WS$_2$ monolayers may be ascribed to distinct features observed in the antisites between impurity atoms and different edge terminations (i.e., sulfur zigzag and tungsten zigzag edges). In addition, An *et al.* [33] demonstrated the formation of W-vacancy lines within single-crystalline triangular WS$_2$ flakes grown under H$_2$-poor conditions, and the mechanism was ascribed to the inhomogeneous accumulation of W precursors along different edges of WS$_2$ [33]. We speculate that these vacancies may serve as hosts for the further incorporation of atomic dopants, leading to the dopant aggregation along these W-vacancy (V_W) lines.

Thus, considering the results reported in this work, we suggest that dark regions in our WS$_2$ monolayers likely occurs during the lateral growth of WS$_2$ flakes due to W-vacancy occupancy, where a higher density of substitutional dopant atoms can be adsorbed on such V_W along the S zigzag edge (perpendicular to the dark region direction), and incorporated into the lattice during the edge propagation. It is worth noting that these dopant atoms possibly are originated from precursor and/or reactor impurities, as has been proposed by previous works [23,75].

IV. CONCLUSION

In summary, the observed *dark regions* in our synthetic WS$_2$ monolayers are regions with a higher concentration of substitutional doping. Our findings are supported by second-harmonic imaging, which identified the *bright regions* as grain boundaries, while no noticeable feature was found in the dark region, and by scanning probe and electronic microscopy. ADF-STEM simulations indicated the formation of different possible substitutional impurities at the W-atom sites. By performing DFT calculations of different possible impurities, we have shown that, excepting Mo, all the other atoms considered introduce midgap states that introduce new radiative recombination mechanisms or charge trapping states. Therefore, we have shown that such substitutional doping is responsible for the substantial quenching of the PL signal. Moreover, DFT calculation also provides a possible mechanism for defect formation along the dark regions. Hence, our work offers a step forward in understanding intrinsic defects in semiconducting 2D materials, which are essential for engineering high-performance optoelectronic devices.

[1] K. F. Mak and J. Shan, Photonics and optoelectronics of 2D semiconductor transition metal dichalcogenides, Nat. Photonics **10**, 216 (2016).

[2] J. R. Schaibley, H. Yu, G. Clark, P. Rivera, J. S. Ross, K. L. Seyler, W. Yao, and X. Xu, Valleytronics in 2D materials, Nat. Rev. Mater. **1**, 16055 (2016).

[3] C. Palacios-Berraquero, M. Barbone, D. Kara, X. Chen, I. Goykhman, D. Yoon, A. Ott, J. Beitner, K. Watanabe, T. Taniguchi, A. Ferrari, and M. Atatüre, Atomically thin quantum light-emitting diodes, Nat. Commun. **7**, 12978 (2016).

[4] A. Branny, S. Kumar, R. Proux, and B. D. Gerardot, Deterministic strain-induced arrays of quantum emitters in a two-dimensional semiconductor, Nat. Commun. **8**, 15053 (2017).

[5] M. Toth and I. Aharonovich, Single photon sources in atomically thin materials, Annu. Rev. Phys. Chem. **70**, 123 (2019).

[6] B. Schuler, K. A. Cochrane, C. Kastl, E. S. Barnard, E. Wong, N. J. Borys, A. M. Schwartzberg, D. F. Ogletree, F. J. G. de Abajo, and A. Weber-Bargioni, Electrically driven photon emission from individual atomic defects in monolayer WS$_2$, Sci. Adv. **6**, eabb5988 (2020).

[7] Q. H. Wang, K. Kalantar-Zadeh, A. Kis, J. N. Coleman, and M. S. Strano, Electronics and optoelectronics of two-dimensional transition metal dichalcogenides, Nat. Nanotechnol. **7**, 699 (2012).

[8] J. Pei, J. Yang, T. Yildirim, H. Zhang, and Y. Lu, Many-body complexes in 2D semiconductors, Adv. Mater. **31**, 1706945 (2019).

[9] S. Najmaei, Z. Liu, W. Zhou, X. Zou, G. Shi, S. Lei, B. I. Yakobson, J.-C. Idrobo, P. M. Ajayan, and J. Lou, Vapour phase growth and grain boundary structure of molybdenum disulphide atomic layers, Nat. Mater. **12**, 754 (2013).

[10] A. L. Elías, N. Perea-López, A. Castro-Beltrán, A. Berkdemir, R. Lv, S. Feng, A. D. Long, T. Hayashi, Y. A. Kim, M. Endo, H. R. Gutiérrez, N. R. Pradhan, L. Balicas, T. E. Mallouk, F. López-Urías, H. Terrones, and M. Terrones, Controlled synthesis and transfer of large-area WS$_2$ sheets: From single layer to few layers, ACS Nano **7**, 5235 (2013).

[11] H. R. Gutiérrez, N. Perea-López, A. L. Elías, A. Berkdemir, B. Wang, R. Lv, F. López-Urías, V. H. Crespi, H. Terrones, and M. Terrones, Extraordinary room-temperature photoluminescence in triangular WS$_2$ monolayers, Nano Lett. **13**, 3447 (2013).

[12] C. Cong, J. Shang, X. Wu, B. Cao, N. Peimyoo, C. Qiu, L. Sun, and T. Yu, Synthesis and optical properties of large-area single-crystalline 2D semiconductor WS$_2$ monolayer from chemical vapor deposition, Adv. Opt. Mater. **2**, 131 (2014).

[13] Y. Zhang, Y. Yao, M. G. Sendeku, L. Yin, X. Zhan, F. Wang, Z. Wang, and J. He, Recent progress in CVD growth of 2D transition metal dichalcogenides and related heterostructures, Adv. Mater. **31**, 1901694 (2019).

[14] A. M. van der Zande, P. Y. Huang, D. A. Chenet, T. C. Berkelbach, Y. You, G.-H. Lee, T. F. Heinz, D. R. Reichman, D. A. Muller, and J. C. Hone, Grains and grain boundaries in highly crystalline monolayer molybdenum disulphide, Nat. Mater. **12**, 554 (2013).

[15] W. Zhou, X. Zou, S. Najmaei, Z. Liu, Y. Shi, J. Kong, J. Lou, P. M. Ajayan, B. I. Yakobson, and J.-C. Idrobo, Intrinsic structural defects in monolayer molybdenum disulfide, Nano Lett. **13**, 2615 (2013).

[16] Z. Liu, M. Amani, S. Najmaei, Q. Xu, X. Zou, W. Zhou, T. Yu, C. Qiu, A. G. Birdwell, F. J. Crowne, R. Vajtai, B. I. Yakobson, Z. Xia, M. Dubey, P. M. Ajayan, and J. Lou, Strain and structure heterogeneity in MoS₂ atomic layers grown by chemical vapour deposition, Nat. Commun. **5**, 5246 (2014).

[17] A. Azizi, X. Zou, P. Ercius, Z. Zhang, A. L. Elías, N. Perea-López, G. Stone, M. Terrones, B. I. Yakobson, and N. Alem, Dislocation motion and grain boundary migration in two-dimensional tungsten disulphide, Nat. Commun. **5**, 4867 (2014).

[18] Z. Lin, B. R. Carvalho, E. Kahn, R. Lv, R. Rao, H. Terrones, M. A. Pimenta, and M. Terrones, Defect engineering of two-dimensional transition metal dichalcogenides, 2D Mater. **3**, 022002 (2016).

[19] H. Nan, Z. Wang, W. Wang, Z. Liang, Y. Lu, Q. Chen, D. He, P. Tan, F. Miao, X. Wang, J. Wang, and Z. Ni, Strong photoluminescence enhancement of MoS₂ through defect engineering and oxygen bonding, ACS Nano **8**, 5738 (2014).

[20] H. Liu, J. Lu, K. Ho, Z. Hu, Z. Dang, A. Carvalho, H. R. Tan, E. S. Tok, and C. H. Sow, Fluorescence concentric triangles: A case of chemical heterogeneity in WS₂ atomic monolayer, Nano Lett. **16**, 5559 (2016).

[21] M. S. Kim, S. J. Yun, Y. Lee, C. Seo, G. H. Han, K. K. Kim, Y. H. Lee, and J. Kim, Biexciton emission from edges and grain boundaries of triangular WS₂ monolayers, ACS Nano **10**, 2399 (2016).

[22] K. M. McCreary, A. T. Hanbicki, S. Singh, R. K. Kawakami, G. G. Jernigan, M. Ishigami, A. Ng, T. H. Brintlinger, R. M. Stroud, and B. T. Jonker, The effect of preparation conditions on raman and photoluminescence of monolayer WS₂, Sci. Rep. **6**, 35154 (2016).

[23] Y.-C. Lin, S. Li, H.-P. Komsa, L.-J. Chang, A. V. Krasheninnikov, G. Eda, and K. Suenaga, Revealing the atomic defects of WS₂ governing its distinct optical emissions, Adv. Funct. Mater. **28**, 1704210 (2018).

[24] S. Cai, W. Zhao, A. Zafar, Z. Wu, Y. Tao, K. Bi, Z. Wei, Z. Ni, and Y. Chen, Photoluminescence characterization of the grain boundary thermal stability in chemical vapor deposition grown WS₂, Materials Research Express **4**, 106202 (2017).

[25] V. Carozo, Y. Wang, K. Fujisawa, B. R. Carvalho, A. McCreary, S. Feng, Z. Lin, C. Zhou, N. Perea-López, A. L. Elías, B. Kabius, V. H. Crespi, and M. Terrones, Optical identification of sulfur vacancies: Bound excitons at the edges of monolayer tungsten disulfide, Sci. Adv. **3**, e1602813 (2017).

[26] M. Zhou, W. Wang, J. Lu, and Z. Ni, How defects influence the photoluminescence of TMDCs, Nano Res. **14**, 29 (2021).

[27] Z. Hu, J. Avila, X. Wang, J. F. Leong, Q. Zhang, Y. Liu, M. C. Asensio, J. Lu, A. Carvalho, C. H. Sow, and A. H. Castro Neto, The role of oxygen atoms on excitons at the edges of monolayer WS₂, Nano Lett. **19**, 4641 (2019).

[28] X. Xu, T. Schultz, Z. Qin, N. Severin, B. Haas, S. Shen, J. N. Kirchhof, A. Opitz, C. T. Koch, K. Bolotin, J. P. Rabe, G. Eda, and N. Koch, Microstructure and elastic constants of transition metal dichalcogenide monolayers from friction and shear force microscopy, Adv. Mater. **30**, 1803748 (2018).

[29] W. Bao, C. Ko, J. Suh, W. Fan, A. Thwon, Y. Zhang, N. J. Borys, C. Ko, J. Suh, W. Fan, A. Thron, Y. Zhang, A. Buyanin, J. Zhang, S. Cabrini, P. D. Ashby, A. Weber-Bargioni, S. Tongay, S. Aloni, D. F. Ogletree *et al.*, Visualizing nanoscale excitonic relaxation properties of disordered edges and grain boundaries

[30] C. Kastl, R. J. Koch, C. T. Chen, J. Eichhorn, S. Ulstrup, A. Bostwick, C. Jozwiak, T. R. Kuykendall, N. J. Borys, F. M. Toma, S. Aloni, A. Weber-Bargioni, E. Rotenberg, and A. M. Schwartzberg, Effects of defects on band structure and excitons in WS₂ revealed by nanoscale photoemission spectroscopy, ACS Nano **13**, 1284 (2019).

[31] L. Mennel, M. M. Furchi, S. Wachter, M. Paur, D. K. Polyushkin, and T. Mueller, Optical imaging of strain in two-dimensional crystals, Nat. Commun. **9**, 516 (2018).

[32] K. Wang, A. A. Puretzky, Z. Hu, B. R. Srijanto, X. Li, N. Gupta, H. Yu, M. Tian, M. Mahjouri-Samani, X. Gao, A. Oyedele, C. M. Rouleau, G. Eres, B. I. Yakobson, M. Yoon, K. Xiao, and D. B. Geohegan, Strain tolerance of two-dimensional crystal growth on curved surfaces, Sci. Adv. **5**, eaav4028 (2019).

[33] G. H. An, S. J. Yun, Y. H. Lee, and H. S. Lee, Growth mechanism of alternating defect domains in hexagonal WS₂ via inhomogeneous W-precursor accumulation, Small **16**, 2003326 (2020).

[34] B. R. Carvalho, Y. Wang, K. Fujisawa, T. Zhang, E. Kahn, I. Bilgin, P. M. Ajayan, A. M. de Paula, M. A. Pimenta, S. Kar, V. H. Crespi, M. Terrones, and L. M. Malard, Nonlinear dark-field imaging of one-dimensional defects in monolayer dichalcogenides, Nano Lett. **20**, 284 (2020).

[35] F. Zhang, Y. Lu, D. S. Schulman, T. Zhang, K. Fujisawa, Z. Lin, Y. Lei, A. L. Elias, S. Das, S. B. Sinnott, and M. Terrones, Carbon doping of WS₂ monolayers: Bandgap reduction and p-type doping transport, Sci. Adv. **5**, eaav5003 (2019).

[36] C. Koch, Determination of core structure periodicity and point defect density along dislocations, Ph.D. thesis, Arizona State University, 2002.

[37] C. Rueden, C. Dietz, M. Horn, J. Schindelin, B. Northan, M. Berthold, and K. Eliceiri, ImageJ Ops, https://imagej.net/Ops.

[38] P. Hohenberg and W. Kohn, Inhomogeneous electron gas, Phys. Rev. **136**, B864 (1964).

[39] W. Kohn and L. J. Sham, Self-consistent equations including exchange and correlation effects, Phys. Rev. **140**, A1133 (1965).

[40] J. M. Soler, E. Artacho, J. D. Gale, A. García, J. Junquera, P. Ordejón, and D. Sánchez-Portal, The SIESTA method for *ab initio* order-*N* materials simulation, J. Phys.: Condens. Matter **14**, 2745 (2002).

[41] E. Artacho, D. Sánchez-Portal, P. Ordejón, A. García, and J. M. Soler, Linear-scaling ab-initio calculations for large and complex systems, Phys. Status Solidi (b) **215**, 809 (1999).

[42] J. P. Perdew, K. Burke, and M. Ernzerhof, Generalized Gradient Approximation Made Simple, Phys. Rev. Lett. **77**, 3865 (1996).

[43] N. Troullier and J. L. Martins, Efficient pseudopotentials for plane-wave calculations, Phys. Rev. B **43**, 1993 (1991).

[44] D. R. Hamann, M. Schlüter, and C. Chiang, Norm-Conserving Pseudopotentials, Phys. Rev. Lett. **43**, 1494 (1979).

[45] L. Kleinman and D. M. Bylander, Efficacious Form for Model Pseudopotentials, Phys. Rev. Lett. **48**, 1425 (1982).

[46] H. J. Monkhorst and J. D. Pack, Special points for Brillouin-zone integrations, Phys. Rev. B **13**, 5188 (1976).

[47] A. Kokalj, XCrySDen—a new program for displaying crystalline structures and electron densities, J. Mol. Graphics Modell. **17**, 176 (1999).

in monolayer molybdenum disulfide, Nat. Commun. **6**, 7993 (2015).

[48] See Supplemental Material at http://link.aps.org/supplemental/10.1103/PhysRevB.106.115301 for additional experimental and theoretical results.

[49] J. Shang, X. Shen, C. Cong, N. Peimyoo, B. Cao, M. Eginligil, and T. Yu, Observation of excitonic fine structure in a 2D transition-metal dichalcogenide semiconductor, ACS Nano **9**, 647 (2015).

[50] M. Currie, A. T. Hanbicki, G. Kioseoglou, and B. T. Jonker, Optical control of charged exciton states in tungsten disulfide, Appl. Phys. Lett. **106**, 201907 (2015).

[51] S. Pak, J. Lee, Y.-W. Lee, A.-R. Jang, S. Ahn, K. Y. Ma, Y. Cho, J. Hong, S. Lee, H. Y. Jeong, H. Im, H. S. Shin, S. M. Morris, S. Cha, J. I. Sohn, and J. M. Kim, Strain-mediated interlayer coupling effects on the excitonic behaviors in an epitaxially grown MoS_2/ WS_2 van der Waals heterobilayer, Nano Lett. **17**, 5634 (2017).

[52] A. M. Dadgar, D. Scullion, K. Kang, D. Esposito, E. H. Yang, I. P. Herman, M. A. Pimenta, E.-J. G. Santos, and A. N. Pasupathy, Strain engineering and Raman spectroscopy of monolayer transition metal dichalcogenides, Chem. Mater. **30**, 5148 (2018).

[53] H. J. Conley, B. Wang, J. I. Ziegler, R. F. Haglund, S. T. Pantelides, and K. I. Bolotin, Bandgap engineering of strained monolayer and bilayer Mos_2, Nano Lett. **13**, 3626 (2013).

[54] Z. Li, Y. Lv, L. Ren, J. Li, L. Kong, Y. Zeng, Q. Tao, R. Wu, H. Ma, B. Zhao, D. Wang, W. Dang, K. Chen, L. Liao, X. Duan, X. Duan, and Y. Liu, Efficient strain modulation of 2D materials via polymer encapsulation, Nat. Commun. **11**, 1151 (2020).

[55] S. B. Desai, G. Seol, J. S. Kang, H. Fang, C. Battaglia, R. Kapadia, J. W. Ager, J. Guo, and A. Javey, Strain-induced indirect to direct bandgap transition in multilayer WSe_2, Nano Lett. **14**, 4592 (2014).

[56] Q. Zhang, Z. Chang, G. Xu, Z. Wang, Y. Zhang, Z.-Q. Xu, S. Chen, Q. Bao, J. Z. Liu, Y.-W. Mai, W. Duan, M. S. Fuhrer, and C. Zheng, Strain relaxation of monolayer WS_2 on plastic substrate, Adv. Funct. Mater. **26**, 8707 (2016).

[57] J. Lee, S. J. Yun, C. Seo, K. Cho, T. S. Kim, G. H. An, K. Kang, H. S. Lee, and J. Kim, Switchable, tunable, and directable exciton funneling in periodically wrinkled WS_2, Nano Lett. **21**, 43 (2021).

[58] Q. Ma, P. M. Odenthal, J. Mann, D. Le, C. S. Wang, Y. Zhu, T. Chen, D. Sun, K. Yamaguchi, T. Tran, M. Wurch, J. L. McKinley, J. Wyrick, K. Magnone, T. F. Heinz, T. S. Rahman, R. Kawakami, and L. Bartels, Controlled argon beam-induced desulfurization of monolayer molybdenum disulfide, J. Phys.: Condens. Matter **25**, 252201 (2013).

[59] N. Kang, H. P. Paudel, M. N. Leuenberger, L. Tetard, and S. I. Khondaker, Photoluminescence quenching in single-layer MoS_2 via oxygen plasma treatment, J. Phys. Chem. C **118**, 21258 (2014).

[60] W. H. Lin, W. S. Tseng, C. M. Went, M. L. Teague, G. R. Rossman, H. A. Atwater, and N. C. Yeh, Nearly 90 crystals by chemical vapor deposition, ACS Nano **14**, 1350 (2020).

[61] L. M. Malard, T. V. Alencar, A. P. M. Barboza, K. F. Mak, and A. M. de Paula, Observation of intense second harmonic generation from MoS_2 atomic crystals, Phys. Rev. B **87**, 201401(R) (2013).

[62] Y. Li, Y. Rao, K. F. Mak, Y. You, S. Wang, C. R. Dean, and T. F. Heinz, Probing symmetry properties of few-layer MoS_2 and h-BN by optical second-harmonic generation, Nano Lett. **13**, 3329 (2013).

[63] N. Kumar, S. Najmaei, Q. Cui, F. Ceballos, P. M. Ajayan, J. Lou, and H. Zhao, Second harmonic microscopy of monolayer MoS_2, Phys. Rev. B **87**, 161403(R) (2013).

[64] X. Yin, Z. Ye, D. A. Chenet, Y. Ye, K. O'Brien, J. C. Hone, and X. Zhang, Edge nonlinear optics on a MoS_2 atomic monolayer, Science **344**, 488 (2014).

[65] L. Lafeta, A. Corradi, T. Zhang, E. Kahn, I. Bilgin, B. R. Carvalho, S. Kar, M. Terrones, and L. M. Malard, Second- and third-order optical susceptibilities across excitons states in 2D monolayer transition metal dichalcogenides, 2D Mater. **8**, 035010 (2021).

[66] F. B. Sousa, L. Lafeta, A. R. Cadore, P. K. Sahoo, and L. M. Malard, Revealing atomically sharp interfaces of two-dimensional lateral heterostructures by second harmonic generation, 2D Mater. **8**, 035051 (2021).

[67] D. A. Bonnel, *Scanning Probe Microscopy and Spectroscopy* (Wiley, New York, 2001).

[68] Y.-J. Yu, Y. Zhao, S. Ryu, L. E. Brus, K. S. Kim, and P. Kim, Tuning the graphene work function by electric field effect, Nano Lett. **9**, 3430 (2009).

[69] K. A. S. Araujo, L. A. Cury, M. J. S. Matos, T. F. D. Fernandes, L. G. Cançado, and B. R. A. Neves, Electro-optical interfacial effects on a graphene/π-conjugated organic semiconductor hybrid system, Beilstein J. Nanotechnol. **9**, 963 (2018).

[70] H. Mogi, Y. Kobayashi, A. Taninaka, R. Sakurada, T. Takeuchi, S. Yoshida, O. Takeuchi, Y. Miyata, and H. Shigekawa, Scanning tunneling microscopy/spectroscopy on MoS_2 embedded nanowire formed in CVD-grown $Mo_{1-x}W_xS_2$ alloy, Jpn. J. Appl. Phys. **56**, 08LB06 (2017).

[71] B. Schuler, J.-H. Lee, C. Kastl, K. A. Cochrane, C. T. Chen, S. Refaely-Abramson, S. Yuan, E. van Veen, R. Roldán, N. J. Borys, R. J. Koch, S. Aloni, A. M. Schwartzberg, D. F. Ogletree, J. B. Neaton, and A. Weber-Bargioni, How substitutional point defects in two-dimensional WS_2 induce charge localization, spin-orbit splitting, and strain, ACS Nano **13**, 10520 (2019).

[72] Y. Jin, Z. Zeng, Z. Xu, Y.-C. Lin, K. Bi, G. Shao, T. S. Hu, S. Wang, S. Li, K. Suenaga, H. Duan, Y. Feng, and S. Liu, Synthesis and transport properties of degenerate p-type Nb-doped WS_2 monolayers, Chem. Mater. **31**, 3534 (2019).

[73] S. Sasaki, Y. Kobayashi, Z. Liu, K. Suenaga, Y. Maniwa, Y. Miyauchi, and Y. Miyata, Growth and optical properties of Nb-doped WS_2 monolayers, Appl. Phys. Express **9**, 071201 (2016).

[74] S. Li, J. Hong, B. Gao, Y.-C. Lin, H. E. Lim, X. Lu, J. Wu, S. Liu, Y. Tateyama, Y. Sakuma, K. Tsukagoshi, K. Suenaga, and T. Taniguchi, Tunable doping of rhenium and vanadium into transition metal dichalcogenides for two-dimensional electronics, Adv. Sci. **8**, 2004438 (2021).

[75] A. W. Robertson, Y.-C. Lin, S. Wang, H. Sawada, C. S. Allen, Q. Chen, S. Lee, G.-D. Lee, J. Lee, S. Han, E. Yoon, A. I. Kirkland, H. Kim, K. Suenaga, and J. H. Warner, Atomic structure and spectroscopy of single metal (Cr, V) substitutional dopants in monolayer MoS_2, ACS Nano **10**, 10227 (2016).